Topological quantum computation based on chiral Majorana fermions

Biao Lian[a,b,1], Xiao-Qi Sun[b,c,1], Abolhassan Vaezi[b,c], Xiao-Liang Qi[b,c,d], and Shou-Cheng Zhang[b,c,2]

[a]Princeton Center for Theoretical Science, Princeton University, Princeton, NJ 08544-0001; [b]Stanford Center for Topological Quantum Physics, Stanford University, Stanford, CA 94305-4045; [c]Department of Physics, Stanford University, Stanford, CA 94305-4045; and [d]School of Natural Sciences, Institute for Advanced Study, Princeton, NJ 08540

Contributed by Shou-Cheng Zhang, September 5, 2018 (sent for review June 11, 2018; reviewed by Eduardo Fradkin, Naoto Nagaosa, and Fuchun Zhang)

The chiral Majorana fermion is a massless self-conjugate fermion which can arise as the edge state of certain 2D topological matters. It has been theoretically predicted and experimentally observed in a hybrid device of a quantum anomalous Hall insulator and a conventional superconductor. Its closely related cousin, the Majorana zero mode in the bulk of the corresponding topological matter, is known to be applicable in topological quantum computations. Here we show that the propagation of chiral Majorana fermions leads to the same unitary transformation as that in the braiding of Majorana zero modes and propose a platform to perform quantum computation with chiral Majorana fermions. A Corbino ring junction of the hybrid device can use quantum coherent chiral Majorana fermions to implement the Hadamard gate and the phase gate, and the junction conductance yields a natural readout for the qubit state.

quantum computing | topological | Majorana

The chiral Majorana fermion, also known as the Majorana–Weyl fermion, is a massless fermionic particle being its own antiparticle proposed long ago in theoretical physics. The simplest chiral Majorana fermion is predicted in 1D space, where it propagates unidirectionally. In condensed-matter physics, 1D chiral Majorana fermions can be realized as quasiparticle edge states of a 2D topological state of matter (1). A celebrated example is the $p+ip$ chiral topological superconductor (TSC), which carries a Bogoliubov–de Gennes (BdG) Chern number $\mathcal{N}=1$ and can be realized from a quantum anomalous Hall insulator (QAHI) with Chern number $\mathcal{C}=1$ in proximity with an s-wave superconductor (2–5). A QAHI–TSC–QAHI junction implemented this way is predicted to exhibit a half-quantized conductance plateau induced by chiral Majorana fermions (3, 4), which has been recently observed in the Cr-doped $(Bi,Sb)_2Te_3$ thin-film QAHI system in proximity with the Nb superconductor (6). The chiral Majorana fermion could also arise in the Moore–Read state of the fractional quantum Hall effect (7) and topologically ordered states of spin systems (8).

A closely related concept, Majorana zero modes (MZMs), which emerge in the bulk vortices of a $p+ip$ TSC (9) or at the endpoints of a 1D p-wave TSC (10, 11), are known to obey non-Abelian braiding statistics and can be used in fault-tolerant topological quantum computations (12–17). Despite the theoretical progress made during the past decade on using MZMs in universal quantum computation (14–17), due to the localized and point-like nature of MZMs, all existing proposed architectures inevitably require nanoscale design and control of the coupling among MZMs. As an essential step toward topological quantum computing, the braiding of MZMs has not yet been experimentally demonstrated.

In this paper, we propose a platform to implement topologically protected quantum gates at mesoscopic scales, which uses propagation of chiral Majorana fermions with purely electrical manipulations instead of MZMs.

Chiral Majorana Fermion Qubits

The main goal of our proposal is to show that the chiral Majorana fermion edge state of the TSC can be used to realize non-Abelian quantum gate operations on electron states, even if there is no non-Abelian anyon traveling along the edge. Since our proposal is closely related to the braiding of MZMs in vortices of the $p+ip$ TSC, we begin by reviewing this process, as illustrated in Fig. 1*A*. Each vortex supports a single MZM γ_i, and thus two vortices together define two quantum states of a fermion degree of freedom. The MZM operators satisfy the anticommutation relation $\{\gamma_i,\gamma_j\}=\delta_{ij}$. If we define $f_{12}=\frac{1}{2}(\gamma_1+i\gamma_2)$ as a complex fermion number, the two states are labeled by $f_{12}^\dagger f_{12}=0,1$, which corresponds to $i\gamma_1\gamma_2=-1,+1$, respectively. When two vortices are exchanged, the corresponding MZMs also are exchanged. In the process in Fig. 1*A*, we have $\gamma_2\to\gamma_3,\ \gamma_3\to-\gamma_2$. The relative minus sign is necessary to preserve the fermion number parity $i\gamma_2\gamma_3$ of this pair. As a consequence, the eigenstates of $i\gamma_1\gamma_2$ and $i\gamma_3\gamma_4$ evolve to eigenstates of $i\gamma_1\gamma_3$ and $-i\gamma_2\gamma_4$, which are entangled states when written in the original basis of $i\gamma_1\gamma_2$ and $i\gamma_3\gamma_4$. For example, the state $|1\rangle_{12}|0\rangle_{34}$ evolves into $\frac{1}{\sqrt{2}}(|0\rangle_{12}|1\rangle_{34}+|1\rangle_{12}|0\rangle_{34})$. Since the vortices have long-range interaction, the Abelian phase during the braiding may not be well defined, but the non-Abelian unitary operation is robust (12). From the reasoning presented above, one can see that the non-Abelian gate during MZM braiding is a direct consequence of exchanging MZMs γ_2,γ_3. The resulting gate must be non-Abelian because $i\gamma_1\gamma_2$ anticommutes with $i\gamma_1\gamma_3$. Therefore, the same non-Abelian gate can be realized by another physical process that exchanges Majorana fermions, even if no braiding of the non-Abelian anyon is involved. In the following, we show how to obtain a realization of the same gate by making use of chiral Majorana fermion edge states of the TSC and complex chiral fermion edge states of the QAHI.

Significance

We propose a platform of quantum computation using the chiral Majorana fermions on the edges of topological materials. The quantum gates are naturally accomplished by the propagation of chiral Majorana fermions. If realized, its computation speed can be 10^3 faster than the currently existing quantum computation schemes.

Author contributions: X.-L.Q. and S.-C.Z. designed research; B.L., X.-Q.S., and A.V. performed research; and B.L., X.-Q.S., A.V., X.-L.Q., and S.-C.Z. wrote the paper.

Reviewers: E.F., University of Illinois at Urbana–Champaign; N.N., The University of Tokyo and Riken Center for Emergent Matter Science; and F.Z., Kavli Institute for Theoretical Physics China.

The authors declare no conflict of interest.

[1]B.L. and X.-Q.S. contributed equally to this work.

[2]To whom correspondence should be addressed. Email: sczhang@stanford.edu.

This article contains supporting information online at www.pnas.org/lookup/suppl/doi:10.1073/pnas.1810003115/-/DCSupplemental.

Published online October 8, 2018.

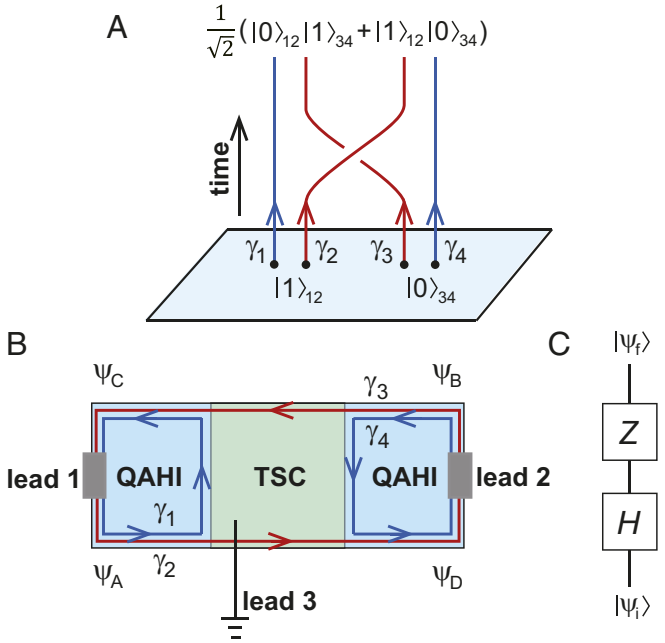

Fig. 1. (*A*) The braiding of vortices in the $p+ip$ TSC. Each pair of vortices supports two states of a single fermion, and the braiding leads to a non-Abelian operation and maps a product state of vortices 12 and 34 into an entangled state, as a consequence of exchanging MZMs γ_2, γ_3. (*B*) Our proposed device of QAHI–TSC–QAHI junction. The same partner switch as in *A* occurs between incoming electrons from leads *A* and *B* and outgoing electrons in leads *C* and *D*. (*C*) Such an exchange leads to a non-Abelian gate that is equivalent to a Hadamard gate *H* followed by a Pauli-*Z* gate *Z*.

The device we propose to study is a 2D QAHI–TSC–QAHI junction predicted in refs. 3 and 4. As shown in Fig. 1*B*, the junction consists of two QAHIs (18–20) of Chern number $\mathcal{C}=1$ and a chiral TSC of BdG Chern number $\mathcal{N}=1$. The conductance σ_{12} is measured between metallic leads 1 and 2 by driving a current I, where no current flows through lead 3 which grounds the TSC. Each edge between the chiral TSC and the vacuum or a QAHI hosts a chiral Majorana fermion edge mode governed by a Hamiltonian $H_M(x)=-i\hbar v_F\gamma(x)\partial_x\gamma(x)$, where $\gamma(x)$ is the Majorana operator satisfying $\gamma(x)=\gamma^\dagger(x)$ and the anticommutation relation $\{\gamma(x),\gamma(x')\}=\delta(x-x')/2$, v_F is the Fermi velocity, and x is the coordinate of the 1D edge. In contrast, each edge between a QAHI and the vacuum hosts a charged chiral fermion (electron) edge mode with a Hamiltonian $H_F(x)=-i\hbar v_F\psi^\dagger(x)\partial_x\psi(x)$, where $\psi(x)$ and $\psi^\dagger(x)$ are the annihilation and creation operators of the edge fermion, and we have assumed chemical potential $\mu=0$ for the moment. By defining two Majorana operators $\gamma_1=(\psi+\psi^\dagger)/2$ and $\gamma_2=(\psi-\psi^\dagger)/2i$ [hereafter $\gamma_i=\gamma_i(x)$ is short for chiral Majorana fermion], one can rewrite $H_F(x)$ as $H_F(x)=-i\hbar v_F(\gamma_1\partial_x\gamma_1+\gamma_2\partial_x\gamma_2)$, which implies a charged chiral fermion mode is equivalent to two chiral Majorana fermion modes. As a result, the edge states of the junction consist of four chiral Majorana fermion modes γ_i $(1\le i\le 4)$ as shown in Fig. 1*B*, which are related to the charged chiral fermion modes on the QAHI edges as $\psi_A=\gamma_1+i\gamma_2$, $\psi_B=\gamma_4+i\gamma_3$, $\psi_C=\gamma_1-i\gamma_3$, and $\psi_D=\gamma_4+i\gamma_2$ (3).

Our key observation is that the same kind of partner switch of Majorana fermions as that of the vortex braiding occurs in this device between incoming and outgoing electrons. An incoming electron from lead A becomes a nonlocal fermion simultaneously on the two edges of the TSC described by γ_1 and γ_2. If we measure the number of outgoing electrons in leads C and D, we find that the outgoing states in the two leads are entangled, because the number operators in these leads do not commute with those of incoming electrons.

To be more specific and to make a connection with quantum computation, consider the low-current limit $I\to 0$ where electrons are injected from lead 1 one by one, each of which occupies a traveling-wave packet state of ψ_A. The occupation number 0 or 1 of such a fermion wave packet state then defines a qubit A with basis $|0_A\rangle$ and $|1_A\rangle$. Similarly, we can define the qubits B, C, and D for ψ_B, ψ_C, and ψ_D, respectively. At each moment of time, the real and imaginary parts of the fermionic annihilation operator of each wave packet state define two self-conjugate Majorana operators localized at the wave packet. When the wave packets move out the superconducting region, they merge with a different partner and form states of the outgoing qubits. In the evolution of the incident electrons, qubits A and B span the Hilbert space of the initial state $|\psi_i\rangle$, while qubits C and D form the Hilbert space of the final state $|\psi_f\rangle$. In the same way as the MZM braiding case, the exchange of γ_2 with γ_3 then leads to a unitary evolution

$$\begin{pmatrix}|0_C0_D\rangle\\|0_C1_D\rangle\\|1_C0_D\rangle\\|1_C1_D\rangle\end{pmatrix}=\frac{1}{\sqrt{2}}\begin{pmatrix}1&0&0&1\\0&1&1&0\\0&-1&1&0\\-1&0&0&1\end{pmatrix}\begin{pmatrix}|0_A0_B\rangle\\|0_A1_B\rangle\\|1_A0_B\rangle\\|1_A1_B\rangle\end{pmatrix}. \quad [1]$$

This transformation should be viewed as an S matrix between incoming and outgoing electron states. Note that the fermion parity is conserved in the unitary evolution. If we define a new qubit $(|0\rangle,|1\rangle)$ in the odd fermion parity subspace as $(|0_A1_B\rangle,|1_A0_B\rangle)$ initially and $(|0_C1_D\rangle,|1_C0_D\rangle)$ at the final time, the above unitary evolution is exactly a topologically protected Hadamard gate H followed by a Pauli-Z gate Z as shown in Fig. 1*C*; namely, $|\psi_f\rangle=ZH\,|\psi_i\rangle$, where

$$H=\frac{1}{\sqrt{2}}\begin{pmatrix}1&1\\1&-1\end{pmatrix},\quad Z=\begin{pmatrix}1&0\\0&-1\end{pmatrix}. \quad [2]$$

The same conclusion holds for the even fermion parity subspace. Therefore, the two qubits A and B (C and D) behave effectively as a single qubit, and we can regard qubit A (C) as the data qubit, while qubit B (D) is a correlated ancilla qubit.

For an electron incident from lead 1 represented by initial state $|\psi_i\rangle=|1_A0_B\rangle$, the junction turns it into a final state $|\psi_f\rangle=(|0_C1_D\rangle+|1_C0_D\rangle)/\sqrt{2}$. This implies (*SI Appendix*) that the entanglement entropy between left and right halves of the junction divided by the dashed line in Fig. 2*A* increases by $\log 2$. Indeed, this is verified by our numerical calculation in

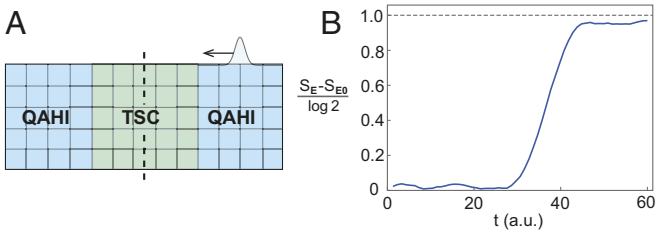

Fig. 2. (*A*) The setup for numerical computation of entanglement entropy. We use a lattice model of QAHI–TSC–QAHI junction, add an initial edge wave packet on a QAHI edge, and then examine the time evolution of the state and the entanglement entropy between the left and the right part of the lattice separated by the dashed line. (*B*) Evolution of entanglement entropy S_E between left and right halves of the junction (divided by dashed line in *A*) with time t (arbitrary unit) after an electron above the Fermi sea is injected from lead 1, where S_{E0} is the entanglement entropy of the Fermi sea.

a lattice model of the junction (Fig. 2*A*), where the entanglement entropy S_E increases with time t as shown in Fig. 2*B*, after an electron is injected from lead 1 above the Fermi sea. More details of this calculation are provided in *SI Appendix*. Since ψ_C and ψ_D propagate into leads 1 and 2, respectively, the electron has $r=1/2$ probability to return to lead 1 and $t=1/2$ probability to tunnel into lead 2. This yields (3) a half-quantized two-terminal conductance $\sigma_{12}=te^2/h=e^2/2h$. Since lead 1 (lead 2) connects ψ_A (ψ_B) with ψ_C (ψ_D) (Fig. 1*B*), we are in fact identifying the charge basis of final qubit C (D) with that of initial qubit A (B). Accordingly, the conductance σ_{12} provides a natural measurement of the overlap probability between $|\psi_i\rangle$ and $|\psi_f\rangle$ under this common basis; namely, $\sigma_{12}=(1-|\langle\psi_f|\psi_i\rangle|^2)e^2/h$.

As we have discussed, the above process is topologically equivalent to fusion and braiding of four vortex operators in the TSC bulk (*SI Appendix*) (21, 22). More concretely, when the electron of an incident state $|1_A0_B\rangle$ reaches the boundary of the TSC, one can imagine an operation of dragging the electron (fermion) into the Hilbert space of two nearby vortices σ_1 and σ_2 in the TSC bulk, after which σ_1 and σ_2 are in the fermionic fusion channel. Meanwhile, one can create two more vortices σ_3 and σ_4 in the bulk of the TSC in the vacuum fusion channel. Next, one can braid the vortices, fuse σ_1 with σ_3, and fuse σ_2 with σ_4. Finally, one can drag the state in the Hilbert space of σ_1 and σ_3 onto the QAH edge of ψ_C and that of σ_2 and σ_4 onto the QAH edge of ψ_D. During such a vortex braiding and fusing process, there is no Majorana fermion propagating on the TSC edge. However, the initial state and the final state in this case are the same as the above process of chiral Majorana fermion propagation (*SI Appendix*), so the two processes are topologically equivalent.

A Testable Quantum Gate

The conductance σ_{12} of the above junction, however, cannot confirm whether chiral Majorana fermions γ_i are coherent or not during the propagation and thus whether the process is a coherent quantum gate. For instance, if a random phase factor is introduced in the propagation of ψ_C and ψ_D, a pure initial state $|\psi_i\rangle=|1_A0_B\rangle$ will evolve into a mixed final state with a density matrix $\rho_f=(|0_C1_D\rangle\langle 0_C1_D|+|1_C0_D\rangle\langle 1_C0_D|)/2$, while the conductance remains $\sigma_{12}=[1-\mathrm{tr}(\rho_f|\psi_i\rangle\langle\psi_i|)]e^2/h=e^2/2h$.

To confirm whether the system as a quantum gate is coherent, we propose to implement a Corbino geometry QAHI–TSC–QAHI–TSC junction as shown in Fig. 3*A* and measure the conductance σ_{12} between lead 1 and lead 2. The junction can

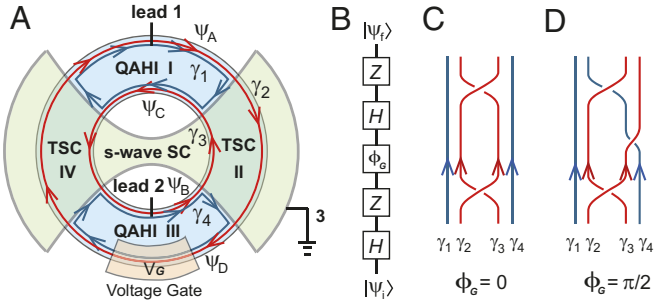

Fig. 3. Quantum interference in the QAHI–TSC–QAHI–TSC Corbino junction. (*A*) The Corbino junction consists of a Corbino QAHI ring with a fan-shaped *s*-wave superconductor on top of it which drives regions II and IV into the TSC, and a voltage gate V_G is added at the bottom edge. (*B*) Such a junction is equivalent to a series of single-qubit quantum gates $ZHR_{\phi_G}ZH$, where R_{ϕ_G} is a phase gate controlled by V_G. (*C* and *D*) The MZM braiding process that gives the same gates as the Corbino device with $\phi_G=0$ and $\phi_G=\pi/2$, respectively.

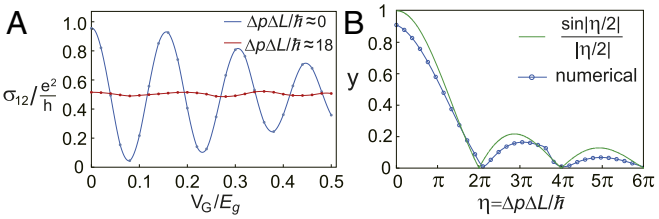

Fig. 4. Numerically calculated σ_{12} oscillation for the Corbino junction. (*A*) σ_{12} calculated for $\Delta p\Delta L/\hbar\approx 0$ and 18 as a function of V_G, respectively. (*B*) The peak-to-valley amplitude y of σ_{12} in units of e^2/h with respect to $\eta=\Delta p\Delta L/\hbar$, which is roughly given by $y=\sin|\eta/2|/|\eta/2|$.

be realized by attaching a fan-shaped *s*-wave superconductor on top of a $\mathcal{C}=1$ QAHI Corbino ring, with a proper out-of-plane magnetic field driving the two regions II and IV into the $\mathcal{N}=1$ TSC phase (4, 6). A voltage gate V_G is added on the bottom edge of QAHI region III covering a length l_G of the edge. Lead 3 grounds the superconductor and has no current passing through. At zero gate voltage, the edge states of the Corbino junction are four chiral Majorana edge states γ_i ($1\le i\le 4$) as shown in Fig. 3*A*.

The gate voltage V_G on the bottom edge of region III behaves as a chemical potential term $H_G=eV_G\psi_D^\dagger\psi_D$ for $\psi_D=\gamma_4+i\gamma_2$ in a length l_G. In the language of quantum computation, this induces a phase gate

$$R_{\phi_G}=\begin{pmatrix}e^{-i\phi_G} & 0\\ 0 & 1\end{pmatrix} \qquad [3]$$

acting on the corresponding qubit D, where the phase shift $\phi_G=eV_Gl_G/\hbar v_F$ is tunable via V_G. Accordingly, the fermion operator ψ_D undergoes a unitary evolution $\psi_D\to e^{i\phi_G}\psi_D$. In particular, when $\phi_G=\pi/2$, this is equivalent to an exchange of Majorana modes γ_2 and γ_4; namely, $\gamma_4\to\gamma_2$, and $\gamma_2\to-\gamma_4$.

If we regard the charged chiral edge modes of QAHI region I (ψ_A and ψ_C) as the data qubit and those of QAHI region III (ψ_B and ψ_D) as the ancilla qubit, the junction can be viewed as a series of quantum gates as shown in Fig. 3*B*, with a total unitary evolution $|\psi_f\rangle=ZHR_{\phi_G}ZH|\psi_i\rangle$. Fig. 3 *C* and *D* shows the MZM braiding process that results in the same non-Abelian gate as the $\phi_G=0$ case and the $\pi/2$ case, respectively. For an electron incident from lead 1 represented by the initial state $|\psi_i\rangle=|1_A0_B\rangle$, the finial state is

$$|\psi_f\rangle=e^{-i\phi_G/2}\left(\cos\frac{\phi_G}{2}|0_A1_B\rangle+i\sin\frac{\phi_G}{2}|1_A0_B\rangle\right). \qquad [4]$$

Therefore, the two-terminal conductance of this Corbino junction is

$$\sigma_{12}=(1-|\langle\psi_f|\psi_i\rangle|^2)\frac{e^2}{h}=\frac{1+\cos\phi_G}{2}\frac{e^2}{h}, \qquad [5]$$

which oscillates as a function of V_G with a peak-to-valley amplitude e^2/h. In contrast, if the system loses coherence completely, the final state will be the maximally mixed state described by density matrix $\rho_f=(|0_A1_B\rangle\langle 0_A1_B|+|1_A0_B\rangle\langle 1_A0_B|)/2$, and the conductance will constantly be $\sigma_{12}=e^2/2h$. Therefore, the oscillation amplitude of σ_{12} measures the coherence of the chiral Majorana fermions in the junction.

So far we have assumed chemical potential $\mu=0$ on all QAHI edges except the interval covered by voltage gate. In general, μ is nonzero and is nonuniform along the QAHI edges when there are disorders. Such a nonzero landscape of μ contributes an additional phase gate, which leads to a phase shift $\phi_G\to\phi_G+\phi_0$,

with ϕ_0 being a fixed phase (*SI Appendix*). Experimentally, the gate voltage V_G and thus ϕ_G can be well controlled by current techniques at a high precision level (23).

Decoherence

There are mainly two effects contributing to the decoherence of chiral Majorana fermions. The first one is the nonmonochromaticity of the incident electron wave packet, which is characterized by a momentum uncertainty $\Delta p \approx 2\pi\hbar/l_W$ for a wave packet of width l_W. In general, the (effective) path lengths of the four chiral Majorana modes γ_i $(1 \le i \le 4)$ in Fig. 3*A* may differ by a length scale ΔL, and the σ_{12} oscillation is sharp only if $\Delta p \Delta L < 2\pi\hbar$. As a demonstration, we numerically examine the time evolution of an electron wave packet from lead 1 within an energy window $v_F[-\Delta p/2, \Delta p/2]$ on a lattice model of the Corbino junction and calculate σ_{12} (*SI Appendix*). Fig. 4*A* shows σ_{12} as a function of V_G/E_g for $\Delta p \Delta L/\hbar \approx 0$ and 18, respectively, where E_g is the QAHI bulk gap. The modulation of the σ_{12} amplitude by V_G is due to the effective change of ΔL as a result of the change in v_F on the edge covered by voltage gate V_G. Fig. 4*B* shows the peak-to-valley amplitude $y = \Delta\sigma_{12}/(e^2/h)$ as a function of $\eta = \Delta p \Delta L/\hbar$, where we find the amplitude roughly decays as $y = |\sin(\eta/2)/(\eta/2)|$. In the experiments, the temperature T yields a momentum uncertainty $\Delta p \approx k_B T/v_F$, where k_B is the Boltzmann constant. For the Cr-doped $(Bi,Sb)_2Te_3$ thin-film QAHI with superconducting proximity studied in ref. 6, the Fermi velocity is of order $\hbar v_F \sim 3$ eV·Å (24), and the temperature T reaches as low as 20 mK. This requires a path-length difference $\Delta L \sim 100$ μm or smaller, which is experimentally feasible (6, 25).

The second effect causing decoherence is the inelastic scattering. The inelastic scattering of charged chiral fermions ψ_i mainly originates from the electron–phonon coupling, which yields an inelastic scattering length $l_{in} \propto T^{-p/2}$ at temperature T (26–28). For integer quantum Hall systems, l_{in} exceeds 10^2μm at $T \sim 20$ mK (29), while l_{in} is expected to be smaller for QAHI (20). In contrast, since the electron–phonon coupling is odd under charge conjugation, the neutral chiral Majorana fermions γ_i are immune to phonon coupling. Instead, their lowest-order local interaction is of the form $\gamma_i \partial_x \gamma_i \partial_x^2 \gamma_i \partial_x^3 \gamma_i$ (30), which is highly irrelevant. Therefore, l_{in} of γ_i in TSCs should be much longer than that of ψ_i in QAHIs. If the σ_{12} interference is to be observed, the sizes of the QAHI and TSC regions in the junction have to be within their inelastic scattering lengths l_{in}, respectively.

Conclusion

In summary, we have introduced the appealing possibility of performing topological quantum computations via propagations of 1D chiral Majorana fermion wave packets, which are physically equivalent to the braiding of MZMs. The Corbino junction above gives a minimal demonstration of single-qubit quantum-gate operations with chiral Majorana fermions, and the conductance of the junction provides a natural readout for the final qubit states. Most importantly, this circumvents two main experimental difficulties in quantum computations with MZMs: the braiding operation of MZMs and the readout of the qubit states. The high velocity of chiral Majorana edge modes also makes the quantum gates 10^3 times faster than those of other quantum computation schemes (31, 32). Furthermore, the development of a single-electron source (33) makes the injection and detection of a single-electron wave packet qubit on edges possible. Yet in the current stage we still face difficulties which are also encountered by the MZM quantum computation scheme: the error correction of the phase gate R_{ϕ_G} (34, 35) and nondemolitional four-Majorana implementation of the controlled not gate (14, 35, 36). If one could overcome these difficulties, one may in principle achieve universal quantum computation using chiral Majorana fermion devices, which would have a high computation speed. Finally, we remark that the conductance oscillation in the Corbino junction, if observed, will also unambiguously prove the existence of quantum coherent chiral Majorana fermions in the experiment (6, 22, 30, 37–39).

ACKNOWLEDGMENTS. B.L. acknowledges the support of the Princeton Center for Theoretical Science at Princeton University. X.-Q.S. and S.-C.Z. acknowledge support from the US Department of Energy, Office of Basic Energy Sciences under Contract DE-AC02-76SF00515. A.V. acknowledges the Gordon and Betty Moore Foundation's Emergent Phenomena in Quantum Systems Initiative through Grant GBMF4302. X.-L.Q. acknowledges support from the David and Lucile Packard Foundation.

1. Qi XL, Zhang SC (2011) Topological insulators and superconductors. *Rev Mod Phys* 83:1057–1110.
2. Qi XL, Hughes TL, Zhang SC (2010) Chiral topological superconductor from the quantum Hall state. *Phys Rev B* 82:184516.
3. Chung SB, Qi XL, Maciejko J, Zhang SC (2011) Conductance and noise signatures of Majorana backscattering. *Phys Rev B* 83:100512.
4. Wang J, Zhou Q, Lian B, Zhang SC (2015) Chiral topological superconductor and half-integer conductance plateau from quantum anomalous Hall plateau transition. *Phys Rev B* 92:064520.
5. Strübi G, Belzig W, Choi MS, Bruder C (2011) Interferometric and noise signatures of Majorana fermion edge states in transport experiments. *Phys Rev Lett* 107:136403.
6. He QL, et al. (2017) Chiral Majorana fermion modes in a quantum anomalous Hall insulator–superconductor structure. *Science* 357:294–299.
7. Moore G, Read N (1991) Nonabelions in the fractional quantum Hall effect. *Nucl Phys B* 360:362–396.
8. Kitaev A (2006) Anyons in an exactly solved model and beyond. *Ann Phys* 321: 2–111.
9. Read N, Green D (2000) Paired states of fermions in two dimensions with breaking of parity and time-reversal symmetries and the fractional quantum Hall effect. *Phys Rev B* 61:10267–10297.
10. Kitaev AY (2001) Unpaired Majorana fermions in quantum wires. *Phys-Usp* 44: 131–136.
11. Lutchyn RM, Sau JD, Das Sarma S (2010) Majorana fermions and a topological phase transition in semiconductor-superconductor heterostructures. *Phys Rev Lett* 105:077001.
12. Ivanov DA (2001) Non-Abelian statistics of half-quantum vortices in *p*-wave superconductors. *Phys Rev Lett* 86:268–271.
13. Kitaev A (2003) Fault-tolerant quantum computation by anyons. *Ann Phys* 303: 2–30.
14. Alicea J, Oreg Y, Refael G, von Oppen F, Fisher MPA (2011) Non-Abelian statistics and topological quantum information processing in 1D wire networks. *Nat Phys* 7: 412–417.
15. Alicea J (2012) New directions in the pursuit of Majorana fermions in solid state systems. *Rep Prog Phys* 75:076501.
16. Aasen D, et al. (2016) Milestones toward Majorana-based quantum computing. *Phys Rev X* 6:031016.
17. Karzig T, et al. (2017) Scalable designs for quasiparticle-poisoning-protected topological quantum computation with Majorana zero modes. *Phys Rev B* 95:235305.
18. Liu CX, Qi XL, Dai X, Fang Z, Zhang SC (2008) Quantum anomalous Hall effect in $Hg_{1-y}Mn_yTe$ quantum wells. *Phys Rev Lett* 101:146802.
19. Yu R, et al. (2010) Quantized anomalous Hall effect in magnetic topological insulators. *Science* 329:61–64.
20. Chang CZ, et al. (2013) Experimental observation of the quantum anomalous Hall effect in a magnetic topological insulator. *Science* 340:167–170.
21. Nayak C, Simon SH, Stern A, Freedman M, Das Sarma S (2008) Non-Abelian anyons and topological quantum computation. *Rev Mod Phys* 80:1083–1159.
22. Bonderson P, Kitaev A, Shtengel K (2006) Detecting non-Abelian statistics in the $\nu = 5/2$ fractional quantum Hall state. *Phys Rev Lett* 96:016803.
23. An S, et al. (2011) Braiding of Abelian and non-Abelian anyons in the fractional quantum Hall effect. arXiv:1112.3400.
24. Liu CX, et al. (2010) Model Hamiltonian for topological insulators. *Phys Rev B* 82:045122.
25. Fox EJ, et al. (2017) Part-per-million quantization and current-induced breakdown of the quantum anomalous Hall effect. arXiv:1710.01850.
26. Thouless DJ (1977) Maximum metallic resistance in thin wires. *Phys Rev Lett* 39: 1167–1169.
27. Pruisken AMM (1988) Universal singularities in the integral quantum Hall effect. *Phys Rev Lett* 61:1297–1300.
28. Huckestein B, Kramer B (1990) One-parameter scaling in the lowest Landau band: Precise determination of the critical behavior of the localization length. *Phys Rev Lett* 64:1437–1440.
29. Koch S, Haug RJ, Klitzing Kv, Ploog K (1991) Size-dependent analysis of the metal-insulator transition in the integral quantum Hall effect. *Phys Rev Lett* 67:883–886.

30. Fu L, Kane CL (2009) Probing neutral Majorana fermion edge modes with charge transport. *Phys Rev Lett* 102:216403.
31. Häffner H, Roos C, Blatt R (2008) Quantum computing with trapped ions. *Phys Rep* 469:155–203.
32. Gambetta JM, Chow JM, Steffen M (2017) Building logical qubits in a superconducting quantum computing system. *npj Quantum Inf* 3:2.
33. Fève G, et al. (2007) An on-demand coherent single-electron source. *Science* 316:1169–1172.
34. Bonderson P, Clarke DJ, Nayak C, Shtengel K (2010) Implementing arbitrary phase gates with Ising anyons. *Phys Rev Lett* 104:180505.
35. Bravyi S, Kitaev A (2005) Universal quantum computation with ideal Clifford gates and noisy ancillas. *Phys Rev A* 71:022316.
36. Bravyi S (2006) Universal quantum computation with the $\nu = 5/2$ fractional quantum Hall state. *Phys Rev A* 73:042313.
37. Akhmerov AR, Nilsson J, Beenakker CWJ (2009) Electrically detected interferometry of Majorana fermions in a topological insulator. *Phys Rev Lett* 102:216404.
38. Stern A, Halperin BI (2006) Proposed experiments to probe the non-Abelian $\nu = 5/2$ quantum Hall state. *Phys Rev Lett* 96:016802.
39. Nilsson J, Akhmerov AR (2010) Theory of non-Abelian Fabry-Perot interferometry in topological insulators. *Phys Rev B* 81:205110.